Enhancing the Resolution of Local Near-Field Probing Measurements With Machine Learning

Emerson K. Cho and Ergun Simsek ⬤, *Senior Member, IEEE*

Abstract— In this purely numerical work, we discuss the use of machine learning (ML) techniques to improve the resolution of local near-field probing (LNFP) measurements when the probe used in LNFP is larger than the device being studied. The study demonstrates that through the implementation of ML algorithms, it is possible to achieve a $\lambda/10$ spatial resolution even with probes that are a few wavelengths wide, while maintaining a maximum relative error of less than 3%. The investigation further reveals that fully connected neural networks (FCNNs) exhibit superior accuracy compared to linear regression when dealing with limited training datasets. Conversely, for larger training datasets, it is unnecessary to construct and train neural networks, as linear regressions prove to be both sufficient and efficient. These findings establish the potential of employing similar ML approaches to enhance the resolution of measurements obtained from diverse experimental setups.

Index Terms— Local near-field probing (LNFP), machine learning (ML), resolution.

I. Introduction

LOCAL near-field probing (LNFP) is a technique that enables the measurement of electric field distributions in microwave and photonic devices with high spatial resolution [1], [2], [3], [4], [5], [6], [7], provided that the probe size is smaller than the dimensions of the device under investigation.

There are various variations of the LNFP technique, including apertureless [1], [2], [3], [4], [5], [6] and aperture-based [7] methods. In the apertureless method, the probe tip is usually a small metallic tip. As the probe tip is brought closer to the device, the electric field causes a shift in the resonance frequency of the probe tip. By measuring the frequency shift at different points along the device, the electric field distribution can be mapped out with high spatial resolution. In the aperture-based method, the probe tip is a small aperture that allows microwaves to pass through it and interact with the device being measured. The electric field is measured by detecting the transmitted or reflected microwave signals.
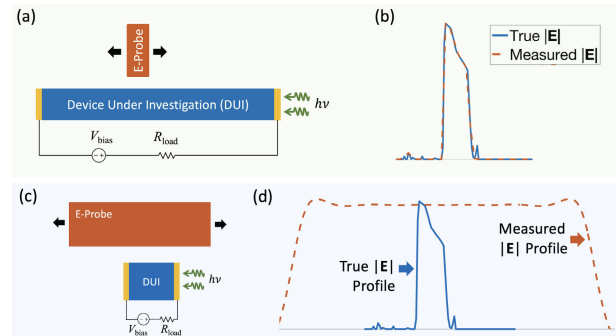
Fig. 1. (a) LNFP setup to measure the electric field where the probe is (a) smaller and (c) larger than the device under investigation. (b) and (d) Typical comparison of true versus measured field intensity for the setups shown in (a) and (c), respectively.

When the probe used in LNFP is smaller than the device being studied, as shown in Fig. 1(a), one can measure the electric field distribution along the device successfully [1], [2], [3], [4], [5], [6], [7], as illustrated in Fig. 1(b). However, if the probe is wider than the device, as depicted in Fig. 1(c), since the resolution of LNFP is limited by the size of the probe and the distance between the probe and the sample surface, it leads to resolution issues as illustrated in Fig. 1(d).

Several methods exist to improve the resolution of LNFP in such situations. For example, imaging algorithms can be employed to process the data collected by LNFP, which can aid in improving the resolution. Deconvolution algorithms [8], [9], [10], for instance, can be utilized to mitigate the effects of probe size and distance from the device. In this study, we adopt a different approach, namely a machine learning (ML) approach, to predict the electric field distribution along a device when the width of a passive electric-field sensing probe exceeds the length of the device under investigation. The specific device we consider in this work is a photodetector but the methods that are discussed below are general and can be applied to any measurement setup.

The present article is structured as follows. First, we describe a simple numerical model that imitates a typical setup used in LNFP measurements. Second, we apply two ML methods, namely linear regression and fully connected neural networks (FCNNs) to predict the true electric field profile inside the device from synthetic LNFP measurement data for
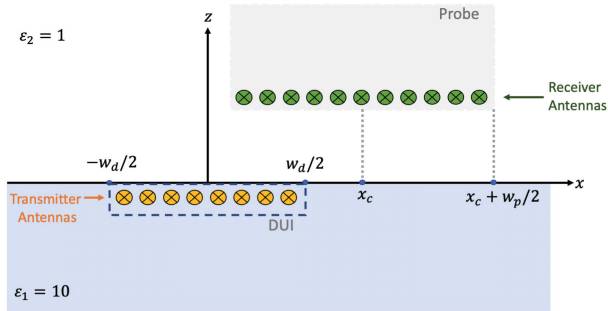
Fig. 2. Illustration of the geometry that aims to mimic E-field measurement with a probe over a device.

Fig. 3. (a) Schematic illustration of a reverse-biased photodetector that is excited from its n-side. The yellow, purple, orange, light gray, dark gray, and dark orange layers represent Au (contacts), InGaAs, InP, InGaAsP Q1.1, InGaAsP Q1.4 layers, and the InP substrate, respectively. (b) Electric field distribution along the photodetector, where the strength is high along the intrinsic (i) region. We can also observe some peaks at the interfaces.

two distinct scenarios. In the first scenario, all devices under scrutiny have a uniform length of 1 μm, and we compare the accuracy and efficiency of the two ML methods as a function of the size of the training dataset. In the second scenario, we analyze a dataset of devices with lengths ranging from 1 to 4 μm. Our findings indicate that when the dataset is extensive, linear regression can make accurate predictions in a few seconds, if not milliseconds. So, there is no need to build and train a neural network. However, the accuracy of FCNNs is almost independent of the dataset size, making them more accurate than linear regression for small training datasets.

II. SIMPLE MATHEMATICAL MODEL TO MIMIC LNFP MEASUREMENTS

Fig. 2 illustrates a simple configuration utilized in this study to imitate an LNFP measurement setup. The device under investigation, which we aim to measure the electric field distribution over via near-field scanning, is centered at the origin with its upper surface positioned at $z = 0$. The width of the device depicted by the dashed black lines is w_d. The gray rectangle represents the probe, with a width of w_p, where $w_p > w_d$, and x_c represents the center of the probe. Since our objective here is to mimic an LNFP measurement, we can simplify matters by disregarding the material properties of the probe, and we can approximately calculate the measured field (E_m) using layered medium Green's functions (LMGFs) as follows.

LMGFs represent the impulse response of a multilayered structure to electrical and magnetic sources [11]. In this context, a planar multilayered medium assumes that layer interfaces are parallel to the xy plane and layer-i is characterized by its relative electrical permittivity ($\epsilon_{r,i}$), conductivity (σ_i), magnetic relative permeability ($\mu_{r,i}$), and layer thickness (t_i). $G_{\eta\zeta}^{EJ}(x, z|x', z')$ type of LMGFs give us the η-component of the electric field at a target point (x, z) due to a Hertzian dipole antenna located at (x', z') pointing toward ζ, where η and ζ are either x, y, or z [11].

If we know the true electric field distribution (E_r) along the device D, then we can assume a finite number of imaginary transmitter antennas that are placed inside the device and use the local electric field intensity as the current driving them. Similarly, we can assume that the fields generated by these imaginary transmitter antennas can be measured by imaginary receiver antennas placed within the probe. If, for instance,
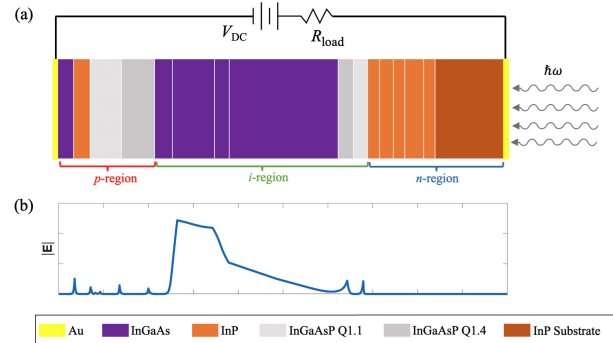
the photodetector is excited with a y-polarized light, then the electric fields established inside the device and measured by the probe are predominantly y-polarized as well. Hence, we can utilize G_{yy}^{EJ}-type LMGFs and approximate the E_m using the following expression:

$$E_m(x_c, z_r) = \int_{x_c-w_p/2}^{x_c+w_p/2} \int_{-w_d/2}^{w_d/2} E_r(x', z_t) \times G_{yy}^{EJ}(x, z_r|x', z_t)dx'dx \quad (1)$$

where z_t and z_r are the z-coordinates of the imaginary transmitter and receiver antennas inside the device and probe, respectively.

For our numerical study, we selected photodetectors [12], [13], [14], [15] as the device under investigation. By solving the drift-diffusion equations [12] on nonuniform spatial and temporal meshes [13], using monochromatic or broadband excitations [14], we can accurately and efficiently calculate both the field and current distributions along the photodetector. Particularly, with the nonuniform time-stepping capability, we can analyze thousands of photodetectors in a few hours using regular personal computers [14], [15].

To generate a variety of realistic electric field profiles, we created 2330 unique modified uni-traveling wave carrier photodetectors by randomly selecting layer thicknesses and doping levels. The number of layers is 16. The material and doping types are assumed to be the same as those used in [14]. The beam and photodetector diameters are 28 μm. The wavelength of the continuous laser is 1550 nm. The modulation frequency (f_{mod}) and modulation depth are 1 GHz and 4%, respectively, i.e., $P_{in} = P_0 \times [1 + 0.04\cos(2\pi f_{mod}t)]$, where $P_0 = 1$ mW and t is time. As shown in Fig. 3(a), the photodetector is reverse biased at 9 V, and the load resistance is 50 Ω. Fig. 3(b) shows a typical electric field distribution over the photodetector. Other than some peaks occurring at the interfaces, the field strength is typically high only in the intrinsic (i) region. We calculate the electric field profiles with the aforementioned drift-diffusion equations solver [12], [13], [14], [15]. Throughout this work, we will refer to these field profiles as the "true" field profiles.
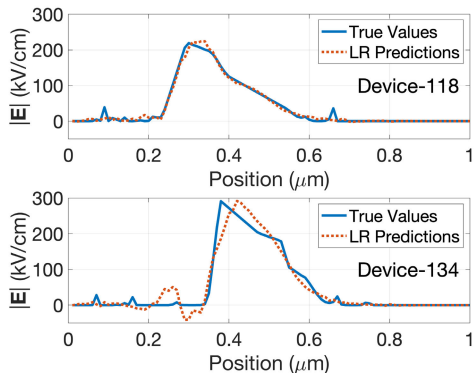
Fig. 4. Electric field profiles: truth (blue solid curves) versus prediction (red dashed curves) obtained with the linear regression model for two randomly selected photodetectors.
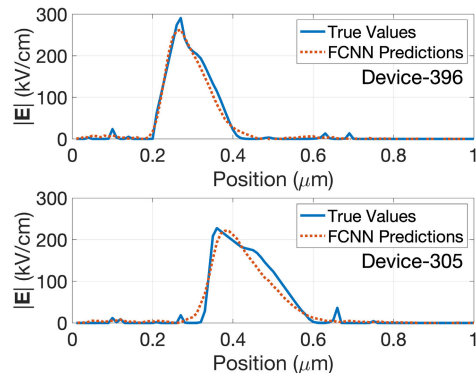

Fig. 5. Electric field profiles: truth (blue solid curves) versus prediction (red dashed curves) obtained with FCNN for two randomly selected photodetectors.

To calculate the LMGFs, we assume the background consists of two layers: the permittivity of the $z < 0$ region is 10, which is the typical value for most semiconductors. The upper layer $z \geq 0$ is air, i.e., $\epsilon_{r,2} = 1$. We assume N_t imaginary transmitter antennas at $z_t = -400$ nm and uniformly spaced between $x = -w_d/2$ and $x = w_d/2$. Additionally, we assume N_r imaginary receiver antennas at $z_r = 400$ nm, uniformly spaced between $x = x_c - w_p/2$ and $x = x_c + w_p/2$, where the probe width, w_p, is 10 μm. Please note that these imaginary antennas are infinitesimal ("ideal") dipole antennas, whose length is much smaller than the wavelength. We determine the parameters N_r and N_t in such a way that the inter-antenna spacings, both inside the device and probe, are close to $\lambda/20$. It is worth mentioning that $\lambda/20$ inter-antenna spacing is commonly used in the computational electromagnetic society to ensure a sufficiently large number of samples for interpolating complex waveforms from a discrete set of solution points.

III. NUMERICAL RESULTS

A. Scenario-1: Constant Device Length

For the sake of simplicity, we first normalize the thickness of each layer of the photodetector such that the total length of each photodetector is 1 μm, i.e., $w_d = 1$ μm. We use two ML algorithms, linear regression, and FCNNs, to predict the true electric field profiles along the photodetectors based on the electric field profiles measured by the probe.[1]

Fig. 4 shows two sample prediction results of the linear regression implementation. In both examples, linear regression successfully predicts the location of the intrinsic layer, where the electric field strength ($|\mathbf{E}|$) is high, the maximum value of $|\mathbf{E}|$, and provides an approximate representation of how $|\mathbf{E}|$ changes inside the intrinsic region. However, even though the training dataset does not include any negative values, the linear regression makes some negative predictions. Despite this significant error from a physical point of view, linear regression can still be considered a useful tool for obtaining a rough estimate of the $|\mathbf{E}|$, considering the fact that it only takes a few milliseconds to make these predictions.

[1]Both the datasets and codes to generate these results can be found at https://github.com/simsekergun/Resolution
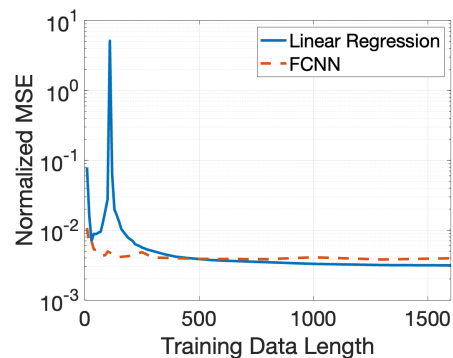

Fig. 6. Normalized mean squared error as a function of training dataset size for linear regression (blue solid curve) and an FCNN (red dotted curve) for a dataset with devices of constant length.

Our FCNN architecture is defined as follows. The input is the blurry electric field measurements, E_m in (1), and the output is the true field profile, E_r in (1). There are four hidden layers between the input and output layers, with each hidden layer containing 800 neurons. Rectified linear unit (ReLU) activation function [16] is employed in all these layers. We utilize a learning rate of 10^{-3} and select Adamax as the optimizer [17]. The loss function is defined using mean squared error. The training process consists of 200 epochs.

Fig. 5 shows two sample prediction results of this FCNN implementation. Once again, we observe accurate predictions of the location of the intrinsic region and the maximum value of $|\mathbf{E}|$. However, in this case, the ML algorithm does not make any negative predictions. In comparison to the linear regression implementation, training the neural network requires a longer duration, i.e., 200 epochs take approximately a minute.

If we define the relative error as the absolute value of the difference between the true (E_{true}) and predicted (E_{pred}) values divided by the $E_{\text{true}} + \xi$, where ξ is a small positive number to avoid a division by zero error, then the average relative error of both approaches is close to $0.03\% \pm 0.01\%$ and the maximum relative error is $2.5\% \pm 0.3\%$.

For the results presented in Figs. 4 and 5, 80% of the data was used for training, while the remaining 20% was used for testing. To investigate the influence of the training dataset size (N_{training}) on the accuracy, we conducted an additional
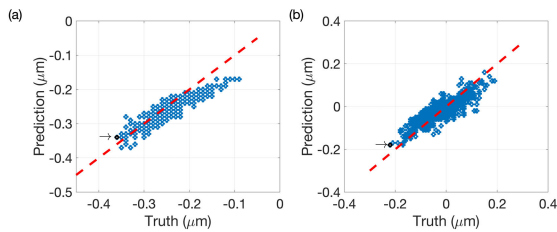
Fig. 7. Each blue circle represents the true versus predicted value, corresponding to (a) left and (b) right boundaries of the photodetector's intrinsic region, for one of the 467 unique photodetector designs used for testing. The red dashed line is the $x = y$ line, typically used in the ML community to demonstrate how accurate (or inaccurate) the predictions are with respect to the true values. Black diamonds represent one of the photodetector designs with a very thin (140 nm) intrinsic region.

Fig. 8. Follows Fig. 6 for a dataset with devices of varying lengths.

set of predictions by varying the N_{training} from 10 to 1600. Fig. 6 illustrates how the mean squared error, normalized with the maximum $|\mathbf{E}|$ of the entire training dataset, changes with N_{training}. We observe that the accuracy of the FCNN remains nearly independent of N_{training} for $N_{\text{training}} \geq 100$, whereas the linear regression implementation yields predictions with a significant amount of errors for some small N_{training} cases, i.e., $N_{\text{training}} < 200$. Considering that each sample in the training dataset holds equal influence over the prediction of the linear regression models, it becomes inevitable to encounter inaccurate predictions, particularly in cases with low correlations between the training and test datasets, especially when N_{training} is relatively small or when the training data includes samples significantly different than the ones in the testing dataset.

To develop an understanding from a resolution point of view, we now focus on the accuracy of the FCNN implementation to predict the boundaries of the intrinsic region, where the electric field strength is high, as illustrated in Fig. 3. In Fig. 7(a) and (b), each blue circle represents the true versus predicted value, where the photodetector's intrinsic region starts and ends, respectively, for one of the 467 unique photodetector designs used for testing. If we had 100% accuracy, all of these blue circles would lie on the $x = y$ line, which is depicted with a red dashed line in each figure. The largest errors occurred for the left boundary (the $p - i$ interface) and for the right boundary (the $i - n$ interface) predictions are 80 and 140 nm, respectively. Considering the excitation wavelength is 1550 nm and the probe width is 10 μm, these "largest error" values might be considered as promising results for converting the blurry measurement results, i.e., the red dashed line in Fig. 2(d), into a profile that is much closer to the true field profile, i.e., the blue solid curve in Fig. 2(d). In Fig. 7, we also highlight one particular photodetector design with black diamonds and arrows. This design's intrinsic region starts at $x = -0.36$ μm and ends at $x = -0.22$ μm. For this 140 nm thin intrinsic region, the ML algorithm's predictions for the left and right boundaries of the intrinsic region are $x = -0.34$ μm and $x = -0.18$ μm. Hence, we can claim that despite using a 6.4λ-wide probe, ML algorithms can enable $\lambda/10$ (or $w_p/64$) resolution. However, we should emphasize that here we are discussing a hypothetical scenario where the probe width is larger than the device under the examination and the sole purpose is to demonstrate that the ML algorithms have the potential to increase the resolution.
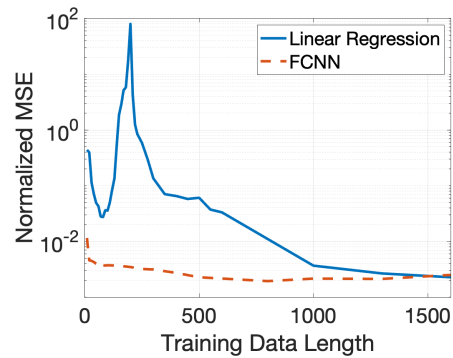
One needs to further investigate the accuracy and efficiency of the ML algorithms for today's advanced near-field microscopy techniques deploying submicrometer probes.

B. Scenario-2: Varying Device Length

In the second scenario, we examine the photodetectors with their original lengths ranging from 1 to 4 μm, i.e., 1 μm $\leq w_d \leq 4$ μm. Employing the same ML models, we observe that when utilizing 80% of the data for training, we can once again achieve highly accurate predictions. However, as depicted in Fig. 8, the accuracy of the linear regression implementation is heavily influenced by N_{training}. It becomes evident that if the training dataset lacks samples similar to those present in the testing dataset, the accuracy of the linear regression models may be significantly compromised. On the other hand, akin to the investigation involving constant device length, the accuracy of the neural network implementation remains almost unaffected by N_{training}. With the utilization of multiple layers and hundreds of neurons, they can effectively learn the underlying patterns, even from small training datasets.

IV. CONCLUSION

We have discussed the utilization of ML techniques to enhance the resolution of LNFP measurements, particularly when the probe employed in LNFP surpasses the size of the device under examination. The results highlight three key findings: 1) with ML, we can achieve a $\lambda/10$ spatial resolution even with few-λ-wide probes, while maintaining a maximum relative error of less than 3%; 2) FCNNs exhibit greater accuracy compared to linear regression models when dealing with small training datasets; and 3) for extensive training datasets, constructing and training a neural network is unnecessary; linear regression proves to be sufficient and efficient. These findings indicate that similar ML approaches can be applied to improve the resolution attained in various measurement setups.

REFERENCES

[1] S. K. Dutta et al., "Imaging microwave electric fields using a near-field scanning microwave microscope," *Appl. Phys. Lett.*, vol. 74, no. 1, pp. 156–158, Jan. 1999.

[2] R. Kantor and I. V. Shvets, "Measurement of electric-field intensities using scanning near-field microwave microscopy," *IEEE Trans. Microw. Theory Techn.*, vol. 51, no. 11, pp. 2228–2234, Nov. 2003.

[3] N. Dehghan, S. Cripps, A. Porch, and J. Lees, "An improved electric field probe with applications in high efficiency PA design and diagnostics," in *Proc. 81st ARFTG Microw. Meas. Conf.*, Seattle, WA, USA, Jun. 2013, pp. 1–4.

[4] M. Farina, D. Mencarelli, A. Di Donato, G. Venanzoni, and A. Morini, "Calibration protocol for broadband near-field microwave microscopy," *IEEE Trans. Microw. Theory Techn.*, vol. 59, no. 10, pp. 2769–2776, Oct. 2011.

[5] R. Hou, M. Spirito, F. Van Rijs, and L. C. N. de Vreede, "Contactless measurement of absolute voltage waveforms by a passive electric-field probe," *IEEE Microw. Wireless Compon. Lett.*, vol. 26, no. 12, pp. 1008–1010, Dec. 2016.

[6] R. Hou, M. Lorenzini, M. Spirito, T. Roedle, F. van Rijs, and L. C. N. de Vreede, "Nonintrusive near-field characterization of spatially distributed effects in large-periphery high-power GaN HEMTs," *IEEE Trans. Microw. Theory Techn.*, vol. 64, no. 11, pp. 4048–4062, Nov. 2016.

[7] D. W. Pohl, L. Novotny, B. Hecht, and H. Heinzelmann, "Radiation coupling and image formation in scanning near-field optical microscopy," *Thin Solid Films*, vol. 273, nos. 1–2, pp. 161–167, Feb. 1996.

[8] P. D. Higgins, C. H. Sibata, L. Siskind, and J. W. Sohn, "Deconvolution of detector size effect for small field measurement," *Med. Phys.*, vol. 22, no. 10, pp. 1663–1666, Oct. 1995.

[9] J. Alda, C. Fumeaux, I. Codreanu, J. A. Schaefer, and G. D. Boreman, "Deconvolution method for two-dimensional spatial-response mapping of lithographic infrared antennas," *Appl. Opt.*, vol. 38, no. 19, pp. 3993–4000, Jul. 1999.

[10] R. Lecaque, S. Grésillon, and C. Boccara, "THz emission Microscopy with sub-wavelength broadband source," *Opt. Exp.*, vol. 16, no. 7, pp. 4731–4738, 2008.

[11] E. Simsek, Q. Huo Liu, and B. Wei, "Singularity subtraction for evaluation of green's functions for multilayer media," *IEEE Trans. Microw. Theory Techn.*, vol. 54, no. 1, pp. 216–225, Jan. 2006.

[12] E. Simsek, I. M. Anjum, and C. R. Menyuk, "Solving drift diffusion equations on non-uniform spatial and temporal domains," in *Proc. Photon. Electromagn. Res. Symp. (PIERS)*, Prague, Czech Republic, Jul. 2023, pp. 1–9.

[13] E. Simsek, I. M. Anjum, T. F. Carruthers, and C. R. Menyuk, "Non-uniform time-stepping for fast simulation of photodetectors under high-peak-power, ultra-short optical pulses," in *Proc. Int. Conf. Numer. Simul. Optoelectronic Devices (NUSOD)*, Sep. 2022, pp. 1–2.

[14] E. Simsek et al., "Fast evaluation of RF power spectrum of photodetectors with windowing functions," *IEEE Trans. Electron Devices*, vol. 70, no. 7, pp. 3643–3648, Jul. 2023, doi: 10.1109/TED.2023.3275553.

[15] E. Simsek, I. M. Anjum, T. F. Carruthers, and C. R. Menyuk, "Designing photodetectors with machine learning," in *Proc. Optica Adv. Photon. Congr.*, Maastricht, The Netherlands, 2022, pp. 1–9.

[16] V. Nair and G. E. Hinton, "Rectified linear units improve restricted Boltzmann machines," in *Proc. IEEE Int. Conf. Mach. Learn. (ICML)*, Feb. 2010, pp. 807–814.

[17] D. P. Kingma and J. Ba, "Adam: A method for stochastic optimization," 2014, *arXiv:1412.6980*.